


# A Modelling Study on Tsunami Propagation in the Caspian Sea

RAÚL PERIÁÑEZ<sup>1</sup>  and CARMEN CORTÉS<sup>2</sup>

*Abstract*—A numerical model that simulates the propagation of tsunamis produced by submarine earthquakes was applied to the Caspian Sea. The model was first applied to the June 1990 (Rudbar) earthquake and our results proved to be coherent with previous simulations. It was also applied to the Krasnovodsk earthquake (1895), which had not been simulated before, and it was found that the coastal area was flooded by a tsunami, as reported in literature. Nevertheless, it was a rather local effect since the tsunami was generated in very shallow waters. Some worst-case hypothetical earthquakes were simulated in the most seismically active regions of the Caspian. In general, both the east and west coasts of the central Caspian Sea would be the most affected by these earthquake-induced tsunamis, with potential significant effects in some cases in cities such as Baku.

**Key words:** Caspian Sea, tsunami, earthquake, numerical simulation.

## 1. Introduction

The Caspian Sea is an area of relatively high seismic activity, determined by its geotectonics. It can be divided into northern, central and southern parts. The last two parts are separated by the so-called Cheleken–Apsheon Threshold (CAT). This is a narrow strip crossing the sea between these two peninsulas from west to east (see Fig. 1) which is characterized by high seismic activity (Kulikov et al. 2014). This high activity has been attributed to normal fault-focal mechanisms related to subduction of the lithosphere as it sinks into the mantle below the northern region of the Caspian Sea (Kadirov and Gadirov 2014). The northern part of the Caspian

basin belongs to the Russian platform, bounded in the south by the Turan platform. The Alpine folded system comprises the central and southern parts of the sea. These regions are separated by deep faults (Kulikov et al. 2014). Details are presented in the cited references and not repeated here.

A large zone of seismic activity is located in the eastern side of the CAT, where high recurrence of strong earthquakes is reported (Dotsenko et al. 2002). Kulikov et al. (2014) and Dotsenko et al. (2002) report other areas of high seismicity where tsunami events have been recorded. They are located in the western side of the Caspian Sea, both south and north of the CAT. Earthquakes produced in the southern Caspian have been studied in detail by Jackson et al. (2002), who provide focal mechanisms for a large number of earthquakes occurred during the second half of the 20th century. Areas where tsunamis have been observed were identified in Dotsenko et al. (2002) and Kulikov et al. (2014), from 17th to 20th centuries.

There is intensive infrastructure development for oil and gas in the Caspian Sea (Kulikov et al. 2014), as well as a nuclear power plant (Aktau, now decommissioned) on the northeast shore. These facilities may constitute a possible source of hazard due to pollution; emissions could be caused by an earthquake and the potential associated tsunami, given the high seismicity of the region, as occurred in the Fukushima Daiichi nuclear power plant (Japan) after the 2011 tsunami (Kaeriyama et al. 2013). In addition to potential pollution events, the damage to infrastructure caused directly by the tsunami waves and consequential high risk to the population living in cities bordering the Caspian Sea should also be considered. Thus, it is relevant to study the characteristics of tsunamis in the Caspian Sea and to

---

<sup>1</sup> Dpto. Física Aplicada I, ETSIA, Universidad de Sevilla, Ctra. Utrera km 1, 41013 Sevilla, Spain. E-mail: rperianez@us.es

<sup>2</sup> Dpto. Matemática Aplicada I, ETSIA, Universidad de Sevilla, Ctra. Utrera km 1, 41013 Sevilla, Spain. E-mail: ccortes@us.es

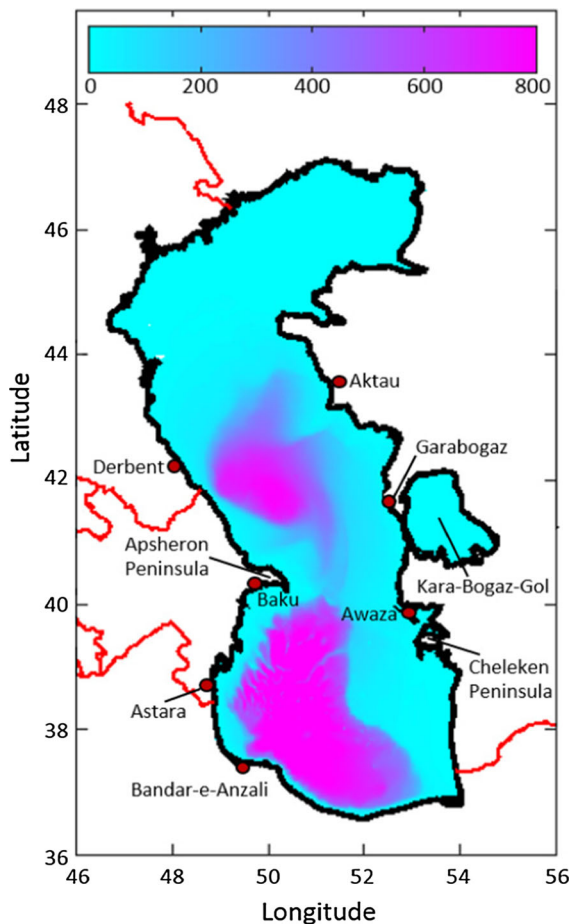


Figure 1

Model domain with water depths (m) and places mentioned in the text. Red lines are political boundaries

estimate the maximum waves which could be expected.

The numerical modelling of tsunami propagation is a relatively well established methodology that has been validated against recorded data from historical events over the world (Choi et al. 2008; Alasset et al. 2006; Ioualalen et al. 2010; Periañez and Abril 2013, 2014; Titov et al. 2016; Abril and Periañez 2017) as well as against laboratory experiments. In spite of this, few modelling works on tsunami propagation in the Caspian Sea can be found in current literature. For instance, Dotsenko et al. (2002) and Kulikov et al. (2014) present some simulations, but for very idealized and non-realistic sources: these authors consider the tsunami source as an ellipse with a reducing water elevation as the distance from the

ellipse center increases. Simulations with a realistic sea floor deformation, for instance as evaluated from the classical Okada (1985) formulation, can be found only (to the authors knowledge) in Salaree and Okal (2015). These authors conducted one simulation for the earthquake occurring in June 20th, 1990, (known as the Rudbar earthquake) in north Iran. They found that the simulated tsunami resulting from this deformation was too weak and did not agree with inundations reported by eye witnesses during a field survey. Thus, the authors concluded that the tsunami was actually produced by a submarine landslide triggered by the earthquake.

This paper is aimed at studying tsunami propagation in the Caspian Sea by adapting previously tested numerical tools (Periañez and Abril 2013, 2014; Abril and Periañez 2017). These numerical exercises are expected to provide some insight into the main characteristics, such as maximum wave amplitude, of the tsunami propagation in this marine system. Initially, the model was applied to the June 20th, 1990 tsunami to compare results with those of Salaree and Okal (2015) and assess its correct customization to the Caspian Sea. Then it was applied to simulate the tsunami triggered by the Krasnovodsk earthquake in July 8th, 1895, magnitude  $M = 7.8$ , (Ambraseys 1997; Balakina and Moskvina 2007), which had not been done before. Finally, some hypothetical tsunamis (based upon realistic sources) occurring in the most seismically active areas of the Caspian Sea were simulated to estimate their potential impacts along the borders of the sea.

The model is briefly described in Sect. 2. Results are described in Sect. 3. A comparison of this model with a previous simulation of the June 20th, 1990 earthquake and tsunami is initially presented. Next, the simulation of the Krasnovodsk tsunami is described. Finally, hypothetical tsunami scenarios are discussed.

## 2. Model Description

The tsunami propagation model is based on 2D depth-averaged barotropic shallow water equations, which describe the propagation of surface shallow water gravity waves. The numerical tool was adapted

from previous works, and proved to be a very robust computational tool. It has been applied to simulate tsunamis in the Atlantic Ocean (Periáñez and Abril 2013), Mediterranean Sea (Periáñez and Abril 2014) and the Red Sea (Abril and Periáñez 2017). It also has been used to simulate the Zanclean Flood of the Mediterranean, an extreme flooding episode (Periáñez and Abril 2015; Abril and Periáñez 2016). A detailed description and involved equations may be seen in these references, and a summary is given in Appendix 1.

The model domain (Fig. 1) extends from 46.0°E to 56.0°E, and from 36.0°N to 47.5°N, with a spatial resolution of 30 seconds of arc. The bathymetry was obtained from the GEBCO08 database, available online. Water depths were corrected to take into account variability of the Caspian Sea level with respect to the ocean (Naderi Beni et al. 2013).

### 3. Results and Discussion

#### 3.1. The June 20th, 1990, Rudbar Tsunami

The Rudbar earthquake, with magnitude  $M_w = 7.4$ , was one of the most destructive earthquakes ever recorded in Iran (Berberian et al. 1992). Several studies were conducted to determine the source mechanism, which are listed in Salaree and Okal (2015). These two authors simulated the

tsunami triggered by this earthquake using the standard Harvard CMT solution for the source (Table 1, HRV source). However, there is no consensus about the geometry of the fault system where the earthquake was produced. Thus, scaling laws which empirically relate the fault size and slip with the earthquake magnitude (Geller 1976) were applied by these authors. Salaree and Okal (2015) also carried out a simulation considering the source as a composition of nine different subevents. Differences between both simulations were negligible. Hence, only a single-event source was applied in the present model, and results are compared with those of Salaree and Okal (2015) to evaluate the correct customization of the model to the Caspian Sea. Nevertheless, there are recent empirical relationships between the fault size and slip with the earthquake magnitude, as for instance those proposed by Wells and Coppersmith (1994) among many others,—see Appendix 2. These equations lead to a slightly larger fault length and smaller width (source HRV2 in Table 1). This source was tested with the present model. The purpose of this additional simulation was simply to investigate whether the differences in source geometry could lead to conclusions other than those of Salaree and Okal (2015).

Results of simulations may be seen in Fig. 2, where only the southern part of the Caspian Sea is shown to allow a better comparison with Fig. 7a in Salaree and Okal (2015). Results using the HRV

Table 1

*Fault parameters used in simulations*

	$M_w$	Depth (km)	$\phi_E^\circ$	$\lambda_N^\circ$	Length (km)	Width (km)	Slip (m)	Strike ( $^\circ$ )	Dip ( $^\circ$ )	Rake ( $^\circ$ )
HRV	7.4	15	49.33	36.96	65	32	1.9	300	73	32
HRV2	7.4	15	49.33	36.96	84	23	2.0	300	73	32
KRA	7.8	20	53.7	39.5	110	40	3.8	292	80	- 90
CAT1	8	33	51.55	40.36	190	35	5.24	299	87	- 86
CAT2	8	55	51.53	40.33	190	35	5.24	332	64	- 64
MIDC1	8	27	48.63	42.72	190	35	5.24	124	88	13
MIDC2	8	82	49.40	41.87	190	35	5.24	101	68	124
MIDC3	8	63	48.70	42.04	190	35	5.24	322	86	- 50
BAK1	8	50	49.94	40.24	190	35	5.24	337	85	- 53
BAK2	8	33	49.95	40.16	190	35	5.24	324	59	- 138

$\phi_E^\circ$  and  $\lambda_N^\circ$  are longitude and latitude, respectively, of the fault center. HRV sources refer to the June 20, 1990 Rudbar earthquake (see text). KRA is the source for the Krasnovodsk earthquake, July 8th, 1895. BAK, CAT and MIDC are variations for sources south the CAT, along the CAT and north the CAT, respectively. Magnitude in the case of KRA should be understood as  $M$ , and depth refers directly to the fault centroid depth in this case

source are essentially the same as in Salaree and Okal (2015): only a narrow band along the southwest shore is affected by the tsunami, and its amplitude (wave maximum height) is extremely small, below 3 cm. Thus, it seems that the present model works correctly for the Caspian Sea.

HRV2 leads to essentially the same results. The differences in amplitudes between both simulations (HRV–HRV2) are also shown in Fig. 2. These differences are of the order of 1 mm over most of the sea. Maximum values are of the order of 1 cm in the southwestern corner of the sea. Consequently, it seems that conclusions of Salaree and Okal (2015) are confirmed: the tsunami triggered directly by the earthquake is too small to agree with visual observations of inundation. Thus, the observed tsunami could have been produced by a submarine landslide triggered by the earthquake, as stated by these authors.

An additional simulation was carried out with a slight variation of the source, as reported in ISC<sup>1</sup> bulletin (event ID is 366754 in this database). This source was obtained by the USGS<sup>2</sup> and implies a larger rake angle (54° instead of 32°), which could enhance the vertical displacements. Nevertheless, results are essentially the same as before (thus they are not shown) and the conclusions above do not change.

After comparing model results with those obtained by a previous calculation using an identical source, the model was used to evaluate the propagation of tsunamis not simulated before.

### 3.2. The Krasnovodsk Earthquake, July 8th, 1895

This was the strongest earthquake of the Transcaspiian region and has been studied in detail by Ambraseys (1997) and Balakina and Moskvina (2007). In this case there is no clear solution for the source due to insufficient amount and quality of seismic data. Thus, plausible values for required parameters have been compiled from information in

<sup>1</sup> International Seismological Centre; <http://www.isc.ac.uk/iscbulletin/search/fmechanisms/interactive/>.

<sup>2</sup> US Geological Survey; <https://earthquake.usgs.gov/earthquakes/search/>.

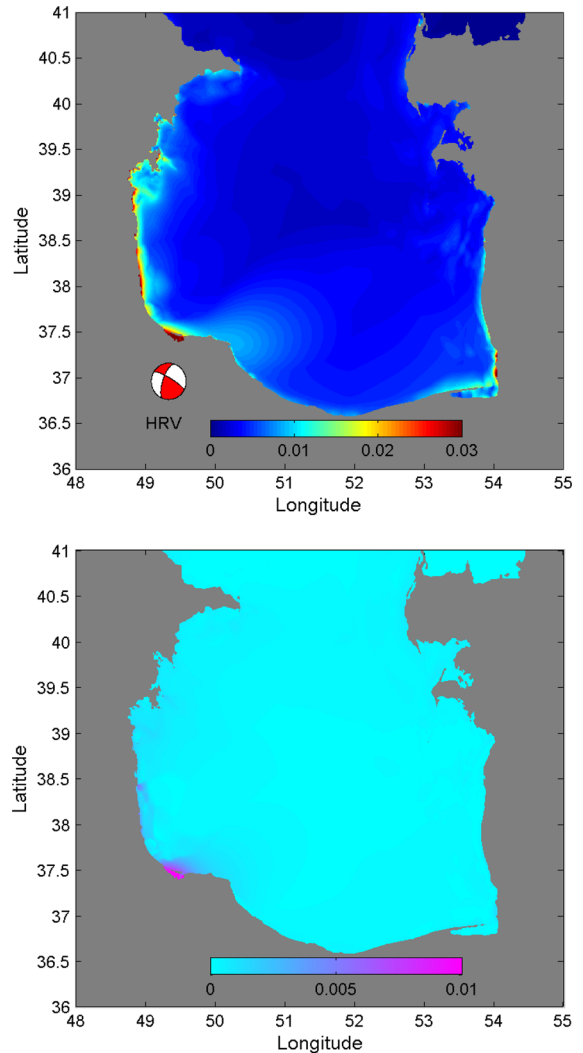


Figure 2

Top: tsunami maximum wave height (m) for the June 20th, 1990 earthquake computed with HRV source. Bottom: differences (m) in amplitudes for this tsunami calculated for HRV and HRV2 sources (HRV–HRV2). A beach ball representing the focal mechanism is drawn at the epicenter location

current literature. According to those authors, the most likely origin of the earthquake is a normal fault in direction WNW and dipping northwards at an angle of 80°. Consequently, strike, dip and rake are fixed as 292°, 80° and –90°, respectively (source KRA in Table 1). Balakina and Moskvina (2007) found that 7.8 is a realistic value for the earthquake magnitude. They add that fault length should be between 100 and 120 km and fault width between 30 and 50 km. Rupture takes place from the surface, thus

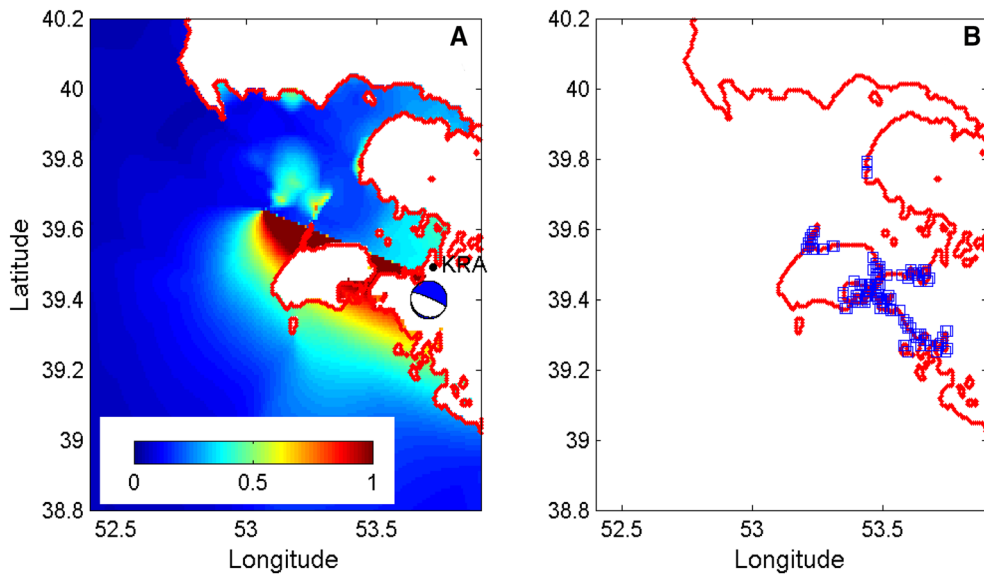


Figure 3

**a** Tsunami maximum wave height (m) for the Krasnovodsk 1895 earthquake. The red line is the reconstructed 1895 coastline. The beach ball corresponding to the source in Table 1 is drawn; the black dot indicates the epicenter location. **b** Blue squares indicate land grid cells which are flooded after the tsunami

20 km may be a realistic value for the fault centroid depth. There is no information about the slip magnitude. A value equal to 3.8 m is obtained using the equations by Wells and Coppersmith (1994) for a magnitude of 7.8, which agrees with the average displacement of 2.5–3.6 m mentioned by Balakina and Moskvina (2007). Parameters are summarized in Table 1. In addition, the sea level was displaced 2 m upwards according to Ambraseys (1997). Actually, the present-day Cheleken Peninsula was then an island. As mentioned in Appendix 1, topography was also corrected due to subsidence or uplift caused by the fault adding the Okada deformation to the original level. This correction may be relevant in calculating inundation for an earthquake occurring inland.

There are no records of field surveys for this tsunami, but only a few historical notes (Kondorskaya and Shebalin 1982; Balakina and Moskvina 2007): after the earthquake, sea waves flooded Cheleken Island and other coastal areas. Thus, it was suggested that the earthquake might have been accompanied by a tsunami (Balakina and Moskvina 2007). This tsunami was simulated for the first time using the source parameters in Table 1.

Figure 3a shows the amplitude of the computed tsunami, together with the 1895 reconstructed coastline. Blue squares in Fig. 3b indicate the grid cells which are flooded by the tsunami. It may be seen that the eastern coast of the Cheleken Peninsula, which was then an island, was flooded. Significant flooding also occurs over the mainland, in front and south of Cheleken Island. This is consistent with information in Balakina and Moskvina (2007). The tsunami amplitude achieves 1.5 m, but only over a very limited area. Its amplitude quickly decreases as the wave propagates into the open waters of the Caspian Sea [according to Green's law (1838)], leading to a negligible effect far from the source area. This behaviour is attributed to its occurrence in very shallow waters.

### 3.3. Hypothetical Tsunami Scenarios

Some hypothetical tsunamis were simulated in three other seismically active regions of the Caspian: the CAT, and south and north of the CAT (these two in the western Caspian Sea). The latter two areas are denoted, respectively, as BAK and MIDC (from Baku and Middle Caspian).

Table 2

*Earthquake ID in ISC database, magnitude, date and time (UTC) for the real earthquakes which have been used as a basis to simulate the hypothetical tsunamis listed in Table 1*

ID	$M_w$	Date	Time	Source in Table 1
2770732	6.8	25/11/2000	18:09	BAK1
1742450	6.5	25/11/2000	18:10	BAK2
499877	6.5	06/03/1986	00:05	CAT1
392584	6.5	16/09/1989	02:05	CAT2
1860504	5.0	05/06/2001	15:33	MIDC1
217463	5.3	31/08/1993	06:55	MIDC2
1734652	4.6	22/04/2000	08:46	MIDC3

The procedure, to allow a simple estimation of the source parameters, was as follows. The largest magnitude earthquakes which have occurred in the areas to date were identified from databases of the ISC bulletin and USGS. These events are listed in Table 2. Focal mechanisms are provided in these databases and their parameters (epicenter location and depth, fault strike, rake and dip) were used in the simulations, but earthquake magnitudes were increased to 8, considered as representative of the worst expected earthquake in the area according to Ulomov (2008). This author states that the largest magnitude of the seismic shock in the Caspian region is not expected to exceed 8. On the other hand, it has been stated that 6.8 may be the minimum magnitude required to trigger a tsunami in the Caspian Sea (Dotsenko et al. 2002)—actually, there is no evidence that the real earthquakes produced any tsunami. The magnitude of 8 was used with the Wells and Coppersmith (1994) relations to deduce the fault size and slip for these hypothetical studies. All sources are detailed in Table 1.

Thus, it has to be kept in mind that these sources remain hypothetical, although based upon real data in these regions.

### 3.3.1 Middle Caspian

According to data collected in the USGS bulletin since 1990, the largest earthquakes identified in this region have magnitudes 5, 5.3 and 4.6 (Table 2). However, as commented above, the earthquake magnitude was increased to 8. The corresponding sources are given in Table 1.

Amplitudes of the generated tsunamis are shown in Fig. 4. The smallest amplitudes occur for MIDC1.

Although this is the shallowest earthquake in this region (27 km), the rake angle of  $13^\circ$  produces a small vertical displacement of the sea floor, thus small waves are generated. In all cases the southern Caspian remains essentially unaffected. The fault strikes prevent energy propagation towards the southeast. Towards the north, the shallow waters produce significant energy dissipation and the wave amplitude reduces (Green 1838); most of the tsunami energy is directed to the west and east shores of the northern Caspian.

### 3.3.2 Cheleken–Apsheron Threshold

The two largest earthquakes identified in this region by the USGS both have magnitudes of 6.5 (Table 2). Again, the earthquake magnitude was increased to 8. The corresponding sources are given in Table 1.

Resulting amplitudes are presented in Fig. 5. Waves are larger in CAT1 than in CAT2. This may be attributed to the fact that the CAT1 earthquake is shallower than CAT2 (33 and 55 km respectively). Also, displacement is more vertical in the case of the CAT1 earthquake. Energy is mainly directed to the east and west in both cases. The entrance of the Karabogaz-Gol is hit by waves around 1 m high in the case of CAT1.

It is also interesting to find that amplitudes in the central part of the southern Caspian are small, but waves are amplified when reaching the southwest corner of the sea. Here they reach heights over 0.5 m.

As an example, some snapshots of water elevations for the CAT1 earthquake are presented in Fig. 6. The western shore (Apsheron Peninsula) of the Caspian is hit by waves a few minutes after the tsunami. In contrast, sea level initially recedes in the eastern shore. There is a slow propagation towards

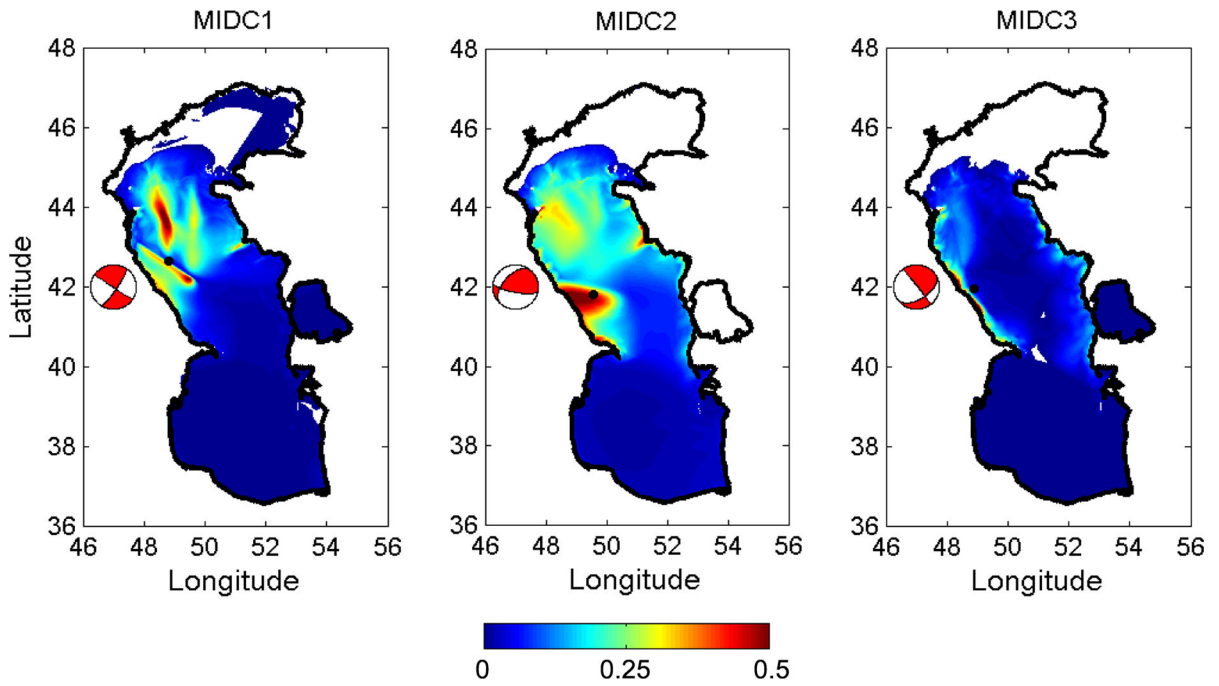


Figure 4

Tsunami maximum wave height (m) for the MIDC1, MIDC2 and MIDC3 sources. The corresponding beach balls to the sources in Table 1 are drawn; the black dots indicate the epicenter location

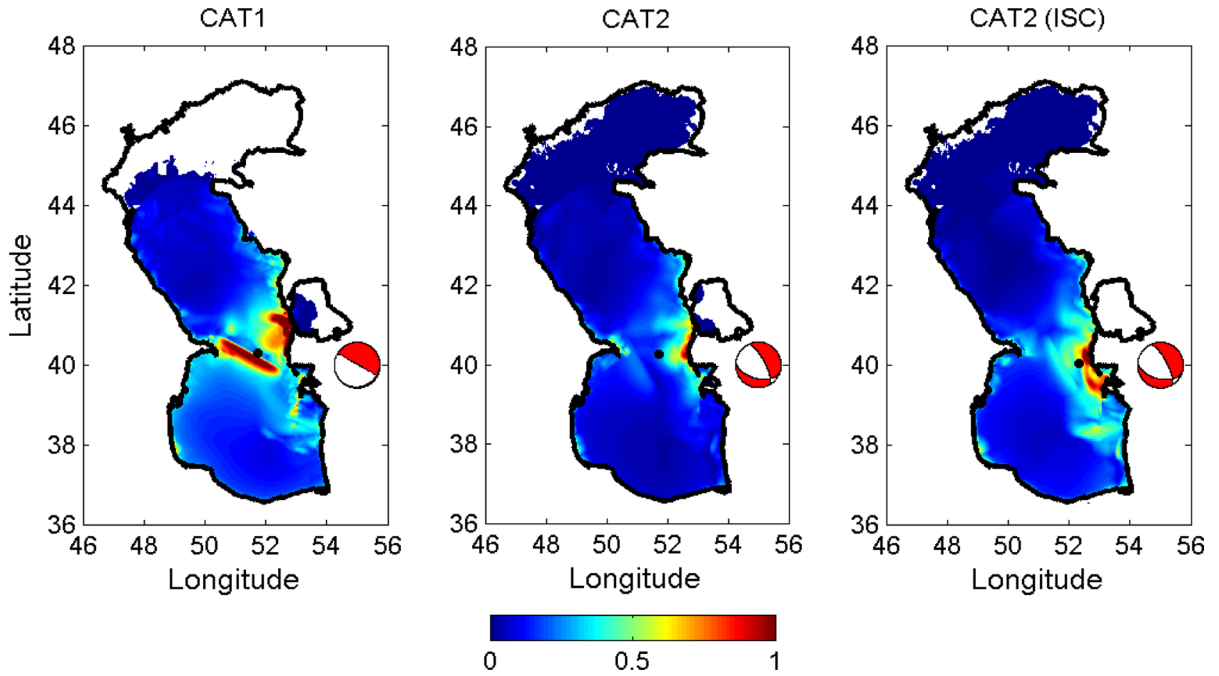


Figure 5

Tsunami maximum wave height (m) for the CAT sources. The ISC map corresponds to CAT2 source but extracted from the ISC bulletin instead of USGS (see text for details). The corresponding beach balls to the sources in Table 1 are drawn; the black dots indicate the epicenter location

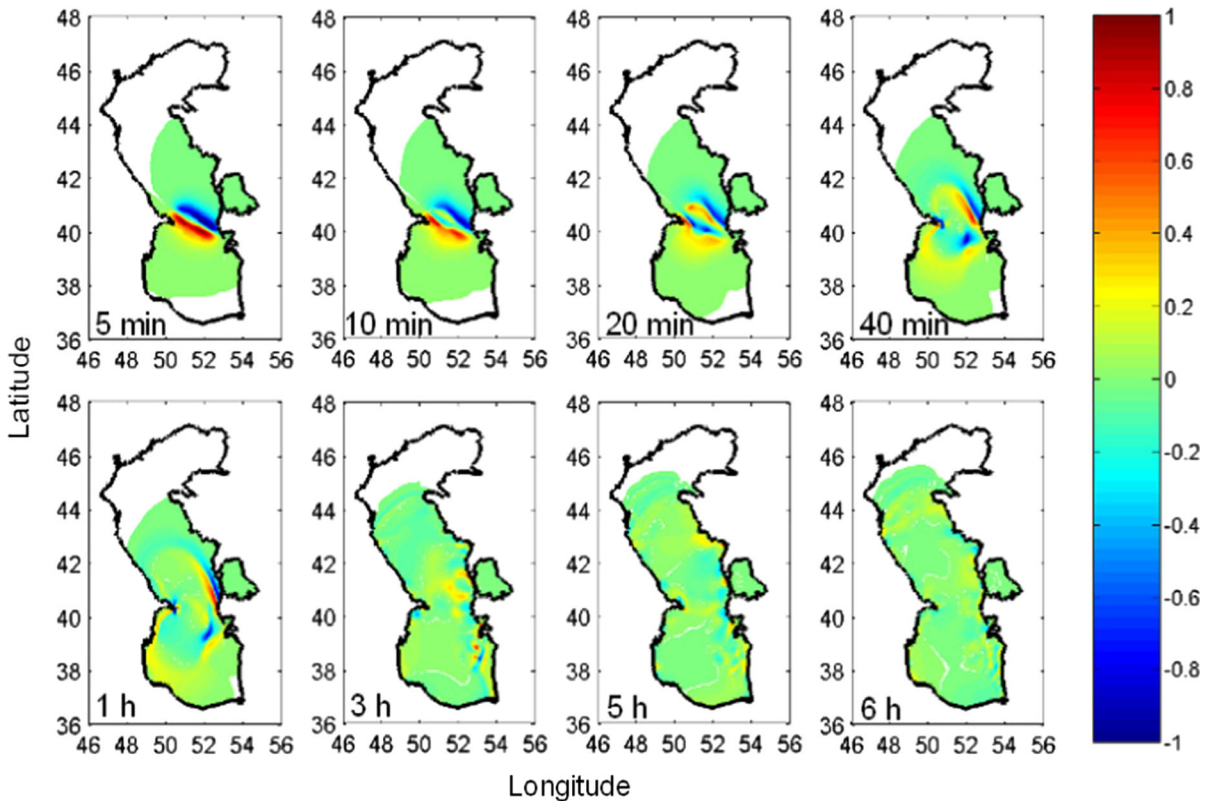


Figure 6  
Snapshots of sea surface elevation (m) for CAT1 source

the north due to the shallower waters here: the first wave front (although small) reaches the 45° latitude after some hours. This is in agreement with the calculations in Dotsenko et al. (2002) with a simple idealized circular tsunami. Propagation towards the south is faster due to the deeper waters of the southern Caspian Sea. The tsunami reaches the south coast in about 1 h.

Another example of results, consisting of time series of water surface elevations with respect to the mean sea level for several coastal locations, can be seen in Fig. 7. An interesting feature is that sea level goes down by about 1 m in Garabogaz, approximately 1.5 h after the earthquake. Then a wave about 80 cm high quickly arrives. More waves arrive about 3 and 5 h after the earthquake. Wave maximum height in Baku is about 40 cm. Here, successive waves arrive with an approximate period of 1.5 h. Amplitudes about 50 cm are also apparent in Awaza; smaller waves reach the other locations.

The focal mechanisms of these earthquakes can also be found in the ISC bulletin. All parameters are the same for CAT1. In the case of CAT2 there is a discrepancy in depth: it is 35 km in ISC instead of the 55 km depth which is defined in USGS (Table 1). Also, the location of the epicenter is slightly different, closer to the shore: 52.17°E, 40.10°N. These changes lead to a higher impact south from Cheleken (Fig. 5).

### 3.3.3 Baku Area

The two largest earthquakes identified in this region in the USGS have magnitudes 6.8 and 6.5 (Table 2). Again, the earthquake magnitude was increased to 8. The corresponding sources are given in Table 1.

Calculated amplitudes are presented in Fig. 8. Waves over 1 m are apparent, and they are slightly larger in BAK2 than in BAK1. As before, this must be attributed to the different depths (50 and 33 km). The largest amplitudes are found in the Apsheron



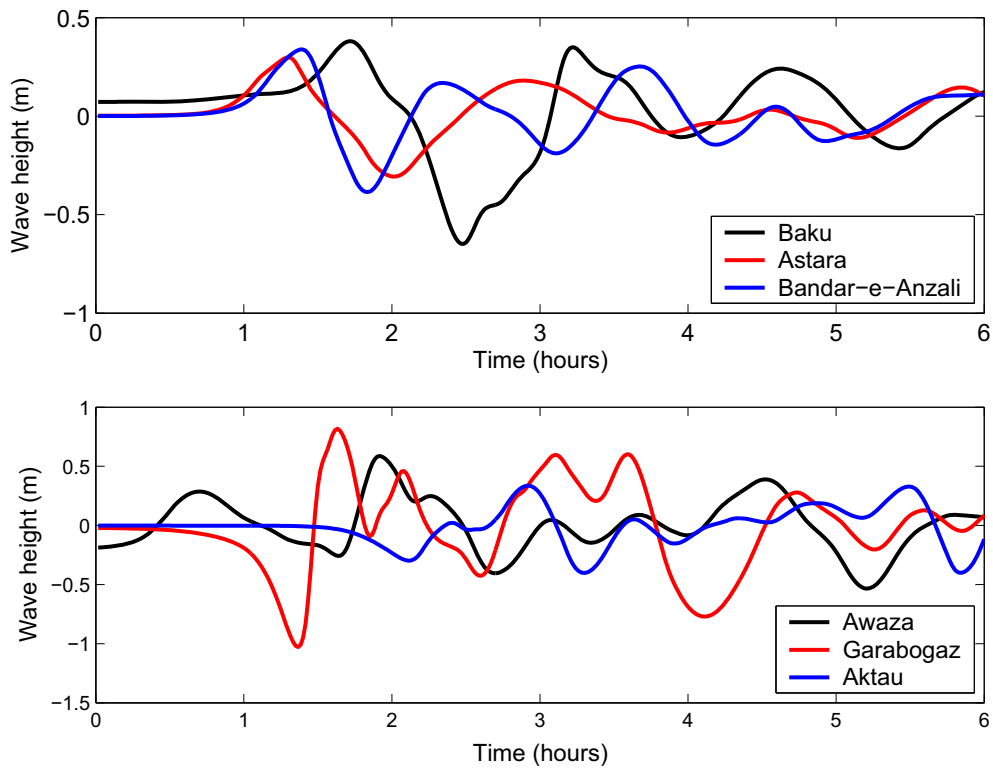


Figure 7  
Time series of sea surface elevation (m) for CAT1 source at several coastal locations. These are shown in Fig. 1

Peninsula since the earthquake epicenter is in this area; in particular, the city of Baku would be affected by this potential tsunami.

#### 4. Conclusions

A numerical model which simulates tsunami propagation, previously tested in other marine areas, was applied to simulate the propagation of tsunamis produced by submarine earthquakes in the Caspian Sea. The case of the June 20, 1990, the Rudbar earthquake was used to compare model results with previous calculations. Our results, in agreement with those, indicated that no significant tsunami was produced by that earthquake. Also, this simulation indicated that the model was appropriately set-up for the Caspian Sea.

The 1895 Krasnovodsk earthquake was simulated for the first time. Results show that the Cheleken peninsula, which was an island at that time, suffered flooding along most of its coast. Significant flooding

also occurs over the mainland, in front and south of Cheleken Island. This is consistent with information in literature. The tsunami amplitude was significant only over a very limited area, quickly decreasing when entering the Caspian Sea open waters. This has to be attributed to the occurrence of the tsunami in very shallow waters.

Some hypothetical earthquakes occurring in the most seismically active areas of the Caspian Sea were simulated. These areas are the Cheleken–Apsheron Threshold and the west side of the Caspian, both north and south of the Cheleken–Apsheron Threshold. In general, both the east and west coasts of the central Caspian Sea would be the most affected by these earthquake-induced tsunamis. Tsunamis generated by earthquakes in the CAT produce the largest impacts in the shore. Tsunamis generated in the MIDC area generally have a very local effect near the source, not propagating to the southern Caspian Sea. In the case of the BAK area, tsunamis generated here

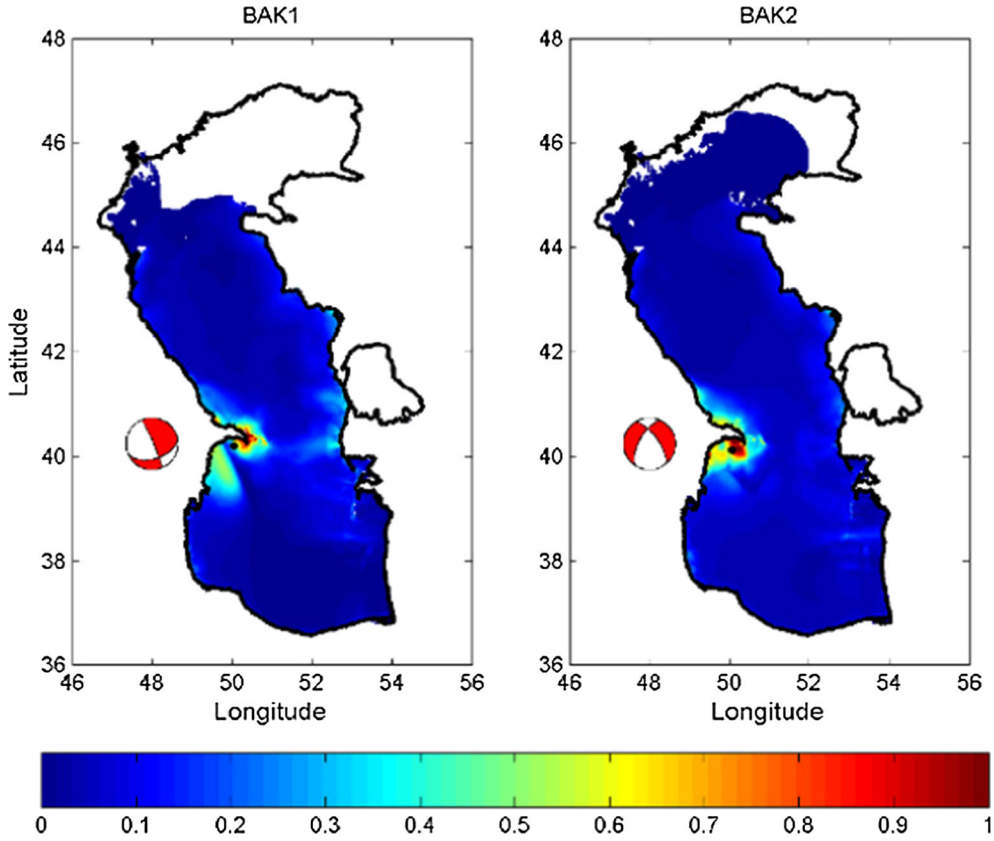


Figure 8

Tsunami maximum wave heights (m) for the BAK sources. The corresponding beach balls to the sources in Table 1 are drawn; the black dots indicate the epicenter location

could produce a significant impact in the close area of the city of Baku.

#### Acknowledgements

The authors are grateful to Mr Andrew Little, Defence Academy of the UK, for kindly reviewing the English of this paper.

#### Appendix 1: Model Description

The 2D depth-averaged barotropic hydrodynamic equations, which describe the propagation of surface shallow water gravity waves, are [see for instance (Kowalik and Murty 1993)]:

$$\frac{\partial \zeta}{\partial t} + \frac{\partial}{\partial x}(Hu) + \frac{\partial}{\partial y}(Hv) = 0; \quad (1)$$

$$\frac{\partial u}{\partial t} + u \frac{\partial u}{\partial x} + v \frac{\partial u}{\partial y} + g \frac{\partial \zeta}{\partial x} - \Omega v + \frac{\tau_u}{\rho H} = A \left( \frac{\partial^2 u}{\partial x^2} + \frac{\partial^2 u}{\partial y^2} \right); \quad (2)$$

$$\frac{\partial v}{\partial t} + u \frac{\partial v}{\partial x} + v \frac{\partial v}{\partial y} + g \frac{\partial \zeta}{\partial y} + \Omega u + \frac{\tau_v}{\rho H} = A \left( \frac{\partial^2 v}{\partial x^2} + \frac{\partial^2 v}{\partial y^2} \right), \quad (3)$$

where  $u$  and  $v$  are the depth averaged water velocities along the  $x$  and  $y$  axis,  $h$  is the depth of water below the mean sea level,  $\zeta$  is the displacement of the water surface above the mean sea level measured upwards,  $H = h + \zeta$  is the total water depth,  $\Omega$  is the Coriolis parameter ( $\Omega = 2\omega \sin \lambda$ , where  $\omega$  is the Earth rotational angular velocity and  $\lambda$  is latitude),  $g$  is acceleration due to gravity,  $\rho$  is a mean value of water density and  $A$  is the horizontal eddy viscosity.  $\tau_u$  and  $\tau_v$  are friction stresses which have been written in terms of a quadratic law:

$$\begin{aligned}\tau_u &= k\rho u\sqrt{u^2 + v^2}; \\ \tau_v &= k\rho v\sqrt{u^2 + v^2},\end{aligned}\quad (4)$$

where  $k$  is the bed friction coefficient. Essentially, these equations express mass and momentum conservation. Parameter values were set to  $k = 0.0015$  and  $A = 10 \text{ m}^2/\text{s}$  (Perianez and Abril 2013, 2014).

All the equations are solved using explicit finite difference schemes (Kowalik and Murty 1993) with second order accuracy. In particular, the MSOU (Monotonic Second Order Upstream) is used for the advective non-linear terms in the momentum equations. Time step is fixed as 5 s to ensure stability.

Boundary conditions have to be specified. There is no water flow towards a dry grid cell. A flood/dry algorithm is required since when the tsunami reaches the coast new wet or dry grid cells may be generated due to run-up or rundown. The numerical scheme described in Kampf (2009) was adopted. Wet grid cells are defined as those with a total water depth  $H$  larger than a threshold value  $H_{\min}$  typically set as a few centimeters. Dry cells are defined as cells where  $H \leq H_{\min}$ . Flooding and drying is implemented in the code via the calculation of the water velocity normal to the interface between wet and dry cells. The calculation is performed when the pressure gradient force is directed towards the dry cell. Otherwise velocity is set to zero at this point. In the case of a non-zero velocity, water level in the dry cell will increase and the cell turns into a wet one once the water depth is larger than  $H_{\min}$ . In the present study,  $H_{\min} = 0.10 \text{ m}$  has been fixed following Kampf (2009) and our previous studies (Perianez and Abril 2013, 2014; Abril and Perianez 2017).

Still waters (zero water elevations and velocities over all the domain) are used as initial conditions across the entire domain, except for those areas affected by the deformation in the free surface induced by the earthquake.

The floor deformation produced by the earthquake is computed using the classical Okada formulae (Okada 1985) through a MATLAB script.<sup>3</sup> Inputs for this equation are fault plane strike, rake, dip, slip,

location, length and width (a rectangular fault is assumed), as well as magnitude of the earthquake and fault centroid depth.

Topography over the domain (both sea and land) is corrected due to subsidence or uplift caused by the fault adding the Okada deformation to the original level. Then, in water cells, the standard procedure assumes that this deformation is instantaneously transferred to the free water surface, and it is imposed as the initial conditions for the numerical simulation, as commented above.

## Appendix 2: Empirical Scaling Relationships

Empirical scaling relationships between the fault size and slip with the earthquake magnitude proposed by Wells and Coppersmith (1994) are:

$$\log L = 0.59M_w - 2.44; \quad (5)$$

$$\log W = 0.32M_w - 1.01; \quad (6)$$

$$\log S = 0.69M_w - 4.80, \quad (7)$$

where  $M_w$  is the earthquake magnitude,  $L$  and  $W$  are the fault length and width (both in km) and  $S$  is the average slip (in m) along the fault.

It should be commented that Stirling et al. (2013) provides scaling laws for the different tectonics of the considered earthquake. However, some of the required laws do not give the values for all parameters which are needed to evaluate deformation according to the Okada (1985) formulae. Consequently, the general laws (which do not differentiate between tectonic regimes) of Wells and Coppersmith (1994) have been used because i) they provide all required parameters (fault length, width and slip) by Okada equations; ii) correlations are better than those of scaling laws, which are specific for given tectonic regimes and iii) the maximum earthquake magnitude used when establishing such specific laws was lower than 8, while the general relations presented above included magnitudes up to 8.1 (note than 8 is the maximum magnitude used in our simulations). In any case, it should be kept in mind that these empirical relations provide only approximations to the real fault geometries.

<sup>3</sup> <https://es.mathworks.com/matlabcentral/fileexchange/25982-okada-surface-deformation-due-to-a-finite-rectangular-source>.

## REFERENCES

- Abril, J. M., & Perri  nez, R. (2016). Revisiting the time scale and size of the Zanclean flood of the Mediterranean (5.33 Ma) from CFD simulations. *Marine Geology*, 382, 242–256.
- Abril, J. M., & Perri  nez, R. (2017). A modelling study on tsunami propagation in the Red Sea: Historical events, potential hazards and spectral analysis. *Ocean Engineering*, 134, 1–12.
- Alasset, P. J., H  bert, H., Maouche, S., Galbini, V., & Meghraoui, M. (2006). The tsunami induced by the 2003 Zemmouri earthquake (MW = 6.9, Algeria): Modelling and results. *Geophysical Journal International*, 166, 213–226.
- Ambraseys, N. N. (1997). The Krasnovodsk (Turkmenistan) earthquake of 8 July 1895. *Journal of Earthquake Engineering*, 1, 293–317.
- Balakina, L. M., & Moskvina, A. G. (2007). Seismogenic zones of the Transcasian Region: characteristics of sources of the largest earthquakes II. The Krasnovodsk and Kazandzhik earthquakes. *Physics of the Solid Earth*, 43, 378–403.
- Berberian, M., Qorashi, M., Jackson, J., Priestley, K., & Wallace, T. (1992). The Rudbar-Tarom earthquake of 20 June 1990 in NW Persia: Preliminary field and seismological observations, and its tectonic significance. *Bulletin of the Seismology Society of America*, 82(4), 1726–1755.
- Choi, B. H., Pelinovsky, E., Kim, D. Ch., Kim, K. O., & Kim, K. H. (2008). Three-dimensional simulation of the 1983 central East (Japan) Sea earthquake tsunami at the Imwon Port (Korea). *Ocean Engineering*, 35, 1545–1559.
- Dotsenko, S.F., Kuzin, I.P., Levin, B.V., & Solovieva, O.N. (2002). Tsunamis in the Caspian Sea: historical events, regional seismicity and numerical modeling. In *Petropavlovks-Kamchatsky Tsunami Workshop*, September 10–15 2002.
- Geller, R. J. (1976). Scaling relations for earthquake source parameters and magnitudes. *Bulletin of the Seismological Society of America*, 66, 1501–1523.
- Green, G. (1838). On the motion of waves in a variable canal of small depth and width. *Transactions of the Cambridge Philosophical Society*, 6, 457–462.
- Ioualalen, M., Arreaga-Vargas, P., Pophet, N., et al. (2010). Numerical modelling of the 26th December 2004 Indian Ocean tsunami for the southeastern coast of India. *Pure and Applied Geophysics*, 167, 1205–1214.
- Jackson, J., Priestley, K., Allen, M., & Berberian, M. (2002). Active tectonics of the South Caspian Basin. *Geophysical Journal International*, 148, 214–245.
- Kadirov, F. A., & Gadirov, A. H. (2014). A gravity model of the deep structure of South Caspian basin along submeridional profile Alborz-Absheron Sill. *Global and Planetary Change*, 114, 66–74.
- Kaeriyama, H., Ambe, D., Shimizu, Y., et al. (2013). Direct observation of <sup>134</sup>Cs and <sup>137</sup>Cs in surface seawater in the western and central North Pacific after the Fukushima Dai-ichi nuclear power plant accident. *Biogeosciences*, 10, 4287–4295.
- Kampf, J. (2009). *Ocean Modelling for Beginners*. Heidelberg: Springer.
- Kondorskaya, N.V., & Shebalin, N.V. (1982). New Catalog of Strong Earthquakes in the USSR from ancient times through 1977. Report SE-31. Translated and Published by World Data Center for Solid Earth Geophysics. NOAA, US.
- Kowalik, Z., & Murty, T. S. (1993). *Numerical modelling of ocean dynamics*. Singapore: World Scientific.
- Kulikov, E. A., Kuzin, I. P., & Yakovenko, O. I. (2014). Tsunamis in the central part of the Caspian Sea. *Oceanology*, 54, 435–444.
- Naderi Beni, A., Lahijani, H., & Harami, R. M. (2013). Caspian sea-level changes during the last millennium: Historical and geological evidence from the south Caspian Sea. *Climate of the Past*, 9, 1645–1665.
- Okada, Y. (1985). Surface deformation due to shear and tensile faults in a half-space. *Bulletin of the Seismological Society of America*, 75, 1135–1154.
- Perri  nez, R., & Abril, J. M. (2013). Modelling tsunami propagation in the Iberia-Africa plate boundary: Historical events, regional exposure and the case-study of the former Gulf of Tartessos. *Journal of Marine Systems*, 111–112, 223–234.
- Perri  nez, R., & Abril, J. M. (2014). Modelling tsunamis in the Eastern Mediterranean Sea. Application to the Minoan Santorini tsunami sequence as a potential scenario for the biblical Exodus. *Journal of Marine Systems*, 139, 91–102.
- Perri  nez, R., & Abril, J. M. (2015). Computational fluid dynamics simulations of the Zanclean catastrophic flood of the Mediterranean (5.33 Ma). *Palaeogeography, Palaeoclimatology, Palaeoecology*, 424, 49–60.
- Salaree, A., & Okal, E. A. (2015). Field survey and modelling of the Caspian Sea tsunami of 1990 June 20. *Geophysical Journal International*, 201, 621–639.
- Stirling, M., Goded, T., Berryman, K., & Litchfield, N. (2013). Selection of Earthquake scaling relationships for seismic-hazard analysis. *Bulletin of the Seismological Society of America*, 103(6), 2993–3011.
- Titov, V., K  nođlu, U., & Synolakis, C. (2016). Development of MOST for real-time tsunami forecasting. *Journal of Waterway, Port, Coastal, and Ocean Engineering*, 142(6), 03116004. [https://doi.org/10.1061/\(ASCE\)WW.1943-5460.0000357](https://doi.org/10.1061/(ASCE)WW.1943-5460.0000357).
- Ulomov, V. I. (2008). Identification of potential spots and long term forecast of strong earthquakes in Northern Caucasus. In A. O. Gliko (Ed.), *Variability of environment and climate. Natural and related technogenic disasters. seismic processes and disasters* (Vol. 1). Moscow: Inst. Fiz., Ross. Akad.
- Wells, D. L., & Coppersmith, K. L. (1994). New empirical relationships among magnitude, rupture width, rupture area and surface displacement. *Bulletin of the Seismological Society of America*, 84, 974–1002.